APL Materials

Lithium-based vertically aligned nancomposite films incorporating $Li_xLa_{0.32}(Nb_{0.7}Ti_{0.32})O_3$ electrolyte with high Li^+ ion conductivity

Cite as: APL Mater. **10**, 051102 (2022); https://doi.org/10.1063/5.0086844
Submitted: 29 January 2022 • Accepted: 11 April 2022 • Published Online: 03 May 2022

Adam J. Lovett, Ahmed Kursumovic, Siân Dutton, et al.

Lithium-based vertically aligned nancomposite films incorporating $Li_xLa_{0.32}(Nb_{0.7}Ti_{0.32})O_3$ electrolyte with high Li^+ ion conductivity

Cite as: APL Mater. 10, 051102 (2022); doi: 10.1063/5.0086844
Submitted: 29 January 2022 • Accepted: 11 April 2022 •
Published Online: 3 May 2022

Adam J. Lovett,[1,a] Ahmed Kursumovic,[1] Siân Dutton,[2] Zhimin Qi,[3] Zihao He,[4] Haiyan Wang,[3] and Judith L. MacManus-Driscoll[1]

AFFILIATIONS

[1]Department of Materials Science and Metallurgy, University of Cambridge, 27 Charles Babbage Road, Cambridge CB3 0FS, United Kingdom
[2]Cavendish Laboratory, University of Cambridge, JJ Thompson Avenue, Cambridge CB3 0HE, United Kingdom
[3]School of Materials Engineering, Purdue University, 701 West Stadium Avenue, West Lafayette, Indiana 47907-2045, USA
[4]School of Electrical Engineering, Purdue University, 701 West Stadium Avenue, West Lafayette, Indiana 47907-2045, USA

Note: This paper is part of the Special Topic on Abundant and Non-toxic Materials for Batteries.
[a]**Author to whom correspondence should be addressed:** ajl207@cam.ac.uk

ABSTRACT

Vertically aligned nanocomposite (VAN) thin films have shown strong potential in oxide nanoionics but are yet to be explored in detail in solid-state battery systems. Their 3D architectures are attractive because they may allow enhancements in capacity, current, and power densities. In addition, owing to their large interfacial surface areas, the VAN could serve as models to study interfaces and solid-electrolyte interphase formation. Here, we have deposited highly crystalline and epitaxial vertically aligned nanocomposite films composed of a $Li_xLa_{0.32\pm0.05}(Nb_{0.7\pm0.1}Ti_{0.32\pm0.05})O_{3\pm\delta}$-$Ti_{0.8\pm0.1}Nb_{0.17\pm0.03}O_{2\pm\delta}$-anatase [herein referred to as LL(Nb, Ti)O-(Ti, Nb)O_2] electrolyte/anode system, the first anode VAN battery system reported. This system has an order of magnitude increased Li^+ ionic conductivity over that in bulk $Li_{3x}La_{1/3-x}NbO_3$ and is comparable with the best available $Li_{3x}La_{2/3-x}TiO_3$ pulsed laser deposition films. Furthermore, the ionic conducting/electrically insulating LL(Nb, Ti)O and electrically conducting (Ti, Nb)O_2 phases are a prerequisite for an interdigitated electrolyte/anode system. This work opens up the possibility of incorporating VAN films into an all solid-state battery, either as electrodes or electrolytes, by the pairing of suitable materials.

INTRODUCTION

All solid-state batteries (ASSBs) utilizing non-flammable electrolytes offer significant advancements in safety while also incorporating materials that enable longer lifespans due to improved chemical and thermal stabilities.[1] However, batteries with planar 2D structures remain constrained by low power and energy densities due to their sluggish ion transport and limited areal interfaces between components of the power source.[2]

An attractive solution to this problem is the incorporation of 3D architectures with significantly enhanced electrode/electrolyte interfaces and shortened ion diffusion path lengths, allowing for significant improvements in power and current densities of ASSBs.[3–5] Vertically aligned nanocomposite (VAN) films, an example of a thin film 3D architecture, have shown promise in oxide solid oxide fuel cells (SOFC) devices displaying enhanced O_2^{2-} ionic conductivity,[6–8] reduced areal surface resistances (ASRs),[9,10] and improved cell performance by enhancing the interfacial surface area.[9] These VAN attributes may be transferrable to ASSBs, enabling improvements in the aforementioned battery properties, while also compensating for intrinsic low diffusivities due to nanoscale path lengths. VANs can be grown with high control of the crystallographic and interface orientation[11] and act as a scaffold to stabilize challenging phases;[12] hence, systems can be optimized to maximize

capacity and performance, particularly when working with materials with anisotropic properties. Thus, VANs may allow a wider selection of materials to be utilized in miniaturized batteries.

To date, there are only two studies of lithium-based VAN films: a $Li_{3x}La_{2/3-x}TiO_3$ (LLTO)-$LiMn_2O_4$ system, not accompanied by any electrochemical characterisation,[13] and a novel VAN-like Li_2MnO_3–Au nanocomposite synthesized using oblate angle deposition in pulsed laser deposition (PLD) to introduce gold columns that enhance electrochemical performance.[14] Hence, the fundamental properties and viability of Li-based VAN films are still poorly understood. There are many suitable candidate materials for battery VAN studies;[15] the electrolytes LLTO and $Li_{3x}La_{1/3-x}NbO_3$ (LLNO) are natural candidates due to their perovskite structure with a/b lattice parameters closely matched to the widely available single crystal substrate, $SrTiO_3$ (STO). LLTO has been subject to extensive PLD studies achieving conductivities of the order 10^{-4}–10^{-5} S cm^{-1}.[16–19] However, this remains 1–2 orders of magnitude lower than reported in bulk,[20–22] usually ascribed to lithium loss and the formation of lithium deficient phases. We note that LLTO does not see widespread use as Ti^{4+} readily undergoes reduction to Ti^{3+} when in contact with lithium metal, which hinders its application. Substituting Nb^{5+} for Ti^{4+} to form LLNO significantly improves the chemical stability against lithium metal.[23] While its bulk conductivity is an order of magnitude lower, in principle, this could be improved using a VAN structure, which is known to lead to improved crystalline perfection and phase stabilisation;[8] consequently, its greater stability vs Li metal may make it a more viable electrolyte in highly crystalline thin film batteries.

Here, we report the successful growth by PLD of an epitaxial LL(Nb, Ti)O-(Ti, Nb)O_2-anatase (matrix-column) VAN films. This is the first electrolyte–anode VAN system reported, complementary to the previous cathode systems.[13,14] We observe exceptional ionic conductivity in the LL(Nb, Ti)O matrix, competitive with the best available planar LLTO thin films and an order of magnitude higher than bulk LLNO. These results may provide a foundation for the development of VAN based ASSBs benefitting from intrinsically high ionic conductivities.

METHODOLOGY

Target preparation

Stoichiometric ratios (50:50 volume ratio) of LLTO ($Li_{0.33}La_{0.55}TiO_3$, Toshima Manufacturing Co., Japan), Nb_2O_5 (99.99%), and 10% weight excess of Li_2O (with respect to LLTO) and combined in a shaker mixer. The sample was pelletized, then sintered for 3 h at 1100 °C in air. After, the target surface was sanded and mounted on an alumina disk.

Pulsed laser deposition

Films were grown by PLD using a KrF excimer laser with a wavelength of 248 nm. Before each deposition, the chamber was evacuated to at least 10^{-5} Pa before filling with oxygen. The target was pre-ablated for 3 min with a fluence of 1.0 J cm^{-2} at 5 Hz. Before growth, substrates were cleaned with acetone in an ultrasonic bath for 5 min and mounted on a substrate carrier with the silver paste (pre-heated at 100 °C).

Highly crystalline and epitaxial VAN films grown on (001) orientated STO/Nb-doped STO (Nb-STO) (0.5 wt. % Nb) were achieved with the following growth conditions: T_{sub} = 880 °C, F = 1.0 J cm^{-2}, pO_2 = 10 Pa, ν = 8 Hz, and substrate–target distance = 45 mm.

XRD characterization

Films were characterized with high resolution x-ray diffraction (XRD) performed on a Panalytical Empyrean vertical diffractometer using a Cu Kα_1 x-ray radiation source with a wavelength of 1.5418 Å.

AFM and CS-AFM characterization

Tapping mode atomic force microscopy (AFM) was performed on selected films using a Brucker Multimode 8 AFM controlled by a Nanoscope (Version 8.15). Current sense AFM (CS-AFM) in a contact mode was performed in the standard top to the bottom bias/measurement configuration using an Agilent 5500 scanning probe microscope with a ±10 V DC bias. Conductive cantilevers were used with Pt–Ir coated tips of nominal 20 nm diameter. IV measurements were collected using an 8 nm diameter Pt tip. The tip was kept at a virtual ground by an inbuilt *trans*-impedance amplifier. The conductive Nb-STO substrate served as the bottom electrode (where DC bias was applied).

TEM

Cross-sectional transmission electron microscopy (TEM) images were taken on a FEI TALOS 200X system with a point-to-point resolution of 1.2 Å. Samples were thinned using a polisher and a dimpler, then transferred to Gatan PIPS II ion milling system to create an electron transparent region for observation. Scanning transmission electron microscopy (STEM) imaging in the high-angle annular dark-field imaging (HAADF) mode, and energy dispersive x-ray spectroscopy (EDX) mapping was also performed on the FEI TALOS 200X system to confirm the elemental distribution.

EIS

Out-of-plane (top to bottom) electrical impedance spectroscopy (EIS) measurements were performed on a 100 nm thick films grown on electronically conducting Nb-STO. A Biologic SP200 potentiostat was used to measure samples with a 50 mV applied AC voltage between 1 Hz and 3 MHz. A LinkAm HFS350 heating stage fitted with probe arms was used to measure EIS between 25 and 100 °C. A ramp rate of 5 °C min^{-1} was used, and the sample was left for 5 min to thermally equilibrate. The samples were mounted on a thin glass slip with the conductive silver paste, which also acted as the bottom electrode. Gold top dot electrodes 300 μm in diameter were deposited by RF sputtering using a shadow mask.

RESULTS AND DISCUSSION

Clear phase separation between highly crystalline epitaxial LL(Nb, Ti)O-(Ti, Nb)O_2 phases in a VAN structure is evident in

high resolution TEM images [Figs. 1(a)–(c)] and STEM-EDX mapping image of Ti [Fig. 1(d)] with highly pure orientated phases affirmed by complimentary x-ray diffraction (XRD) patterns (Fig. 2).

The LL(Nb, Ti)O matrix phase, a solid-state solution of the well-studied LLTO and LLNO electrolytes, forms a dense film with Ti rich (Ti, Nb)O_2 columns uniformly distributed throughout. Symmetric 2θ-ω XRD patterns [Fig. 2(a)] index the matrix to a tetragonal perovskite with c = 7.87 Å, well matched to the LLTO (7.74–7.79 Å[24]) and LLNO (c ≈ 7.79–7.91 Å[25]) phases (Li-content dependent). The presence of Kiessig fringes flanking the perovskite (002) reflection [Fig. 2(b)] and very low intensity (005) and (007) reflections often not resolved in powder XRD [Fig. 2(a)] confirm that the deposited LL(Nb, Ti)O phase is very crystalline. From φ scans [Fig. 2(c)], we confirm that LL(Nb, Ti)O is epitaxially aligned to STO with a [001]LL(Nb, Ti)O//[001]STO relationship. This is expected as $a/b_{LLTO/LLNO} \approx a_{STO}$. Sampling a large area of the dense film using STEM-EDX analysis yields a composition of $Li_xLa_{0.32\pm0.05}(Nb_{0.7\pm0.1}Ti_{0.32\pm0.05})O_{3\pm\delta}$. The c = 7.87 Å lattice parameter determined from 2θ-ω XRD patterns [Fig. 2(a)] is also consistent with a Nb rich LL(Nb, Ti)O phase when considering Vegard's law (predicted c = 7.86 Å for $LLNb_{0.7}Ti_{0.3}O$).

Columnar-structured outgrowths in the diameter of 20–30 nm are clearly seen protruding the surface of the very dense matrix (Fig. 1). The presence of localized titanium matching topography in Ti contrast STEM-HAADF images [Fig. 1(d)] and the indexed 2θ-ω XRD pattern [Fig. 2(a)] confirms the phase to be (00l) orientated TiO_2 anatase (tetragonal, a = 3.789 Å, c = 9.537 Å). The phase has a stoichiometry of $Ti_{0.8\pm0.1}Nb_{0.17\pm0.03}O_{2\pm\delta}$ determined by HAADF STEM EDX. TiO_2 is a widely reported lithium deficient impurity phase in LLTO planar studies, which is detrimental to the performance of such films.[16–18] However, in these LL(Nb, Ti)O-(Ti, Nb)O_2 VAN films, this is not detrimental, as any lithium deficient regions contribute to the VAN architecture, encouraging the formation of (Ti, Nb)O_2 nanocolumns. TiO_2-anatase is an anode that in bulk can intercalate high lithium contents with a theoretical gravimetric charge density of 168 mA h g^{-1} (Ref, 26) and has attracted attention as an alternative to Li metal as it is cheap, widely available, and environmentally benign.[27] We note that the niobium doping of anatase TiO_2 is highly desirable for enhancing the poor electronic conductivity of TiO_2 (as low as 10^{-7}–10^{-12} S cm^{-1} in bulk[28]) to give metallic-type conduction behavior.[29,30] It has been shown that Nb doping of TiO_2 drastically improves the electrochemical performance at high charge/discharge rates,[31] increased capacities,[31,32] and improved cycling stability.[32] Also, nanoparticle anatase TiO_2 (7–120 nm) has shown improved lithium insertion capacity, up to $LiTiO_2$, half a mole increase with respect to bulk, and improved lithium ion solubility with the decreasing particle size.[33,34] The nanocolumns in these VAN films are analog of nanoparticles.

We now consider the excellent Li^+ ionic conductivity of our LL(Nb, Ti)O-(Ti, Nb)O_2 VAN films. Figure 3 displays EIS data of

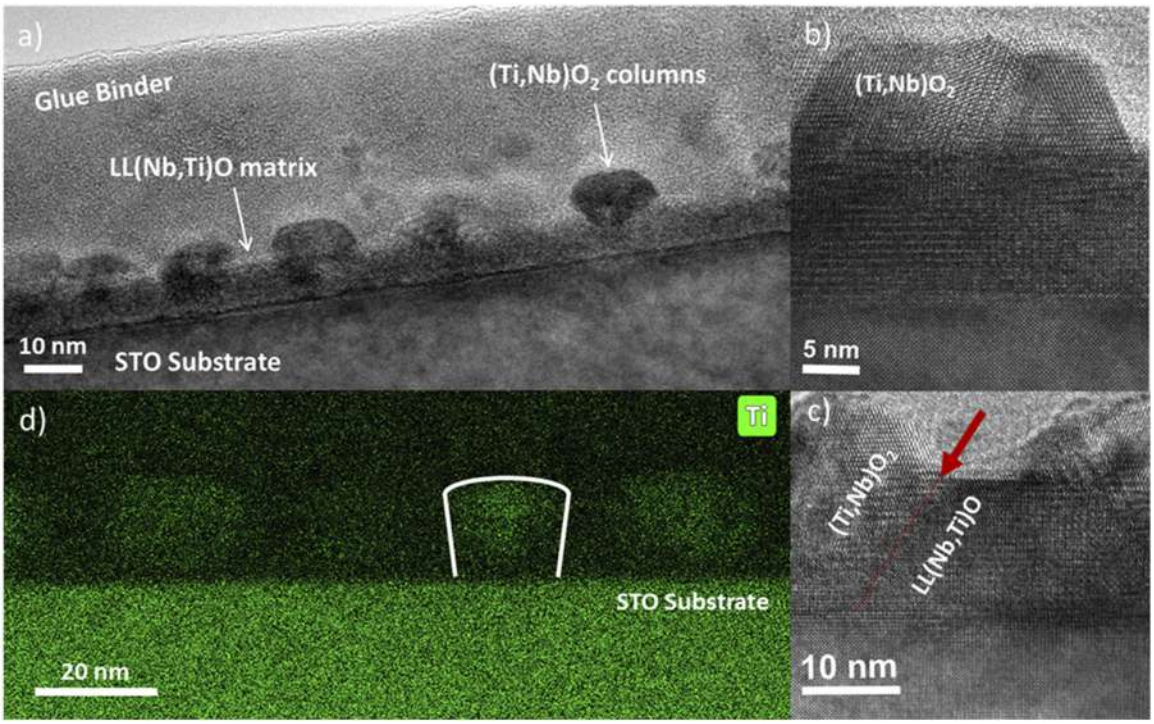

FIG. 1. (a) Cross-sectional TEM images of a nanocomposite thin film composed of pillars of (Ti, Nb)O_2 embedded in a LL(Nb, Ti)O matrix grown on STO (001). (b) and (c) Close-up images of the pillars showing high levels of crystallinity and the clean, crystalline interface between the two phases. The interface between the matrix and column is marked by the red arrow/line. (d) Titanium EDX map of a VAN film, clearly showing localized (Ti, Nb)O_2 columns, an example of which is highlighted in white.

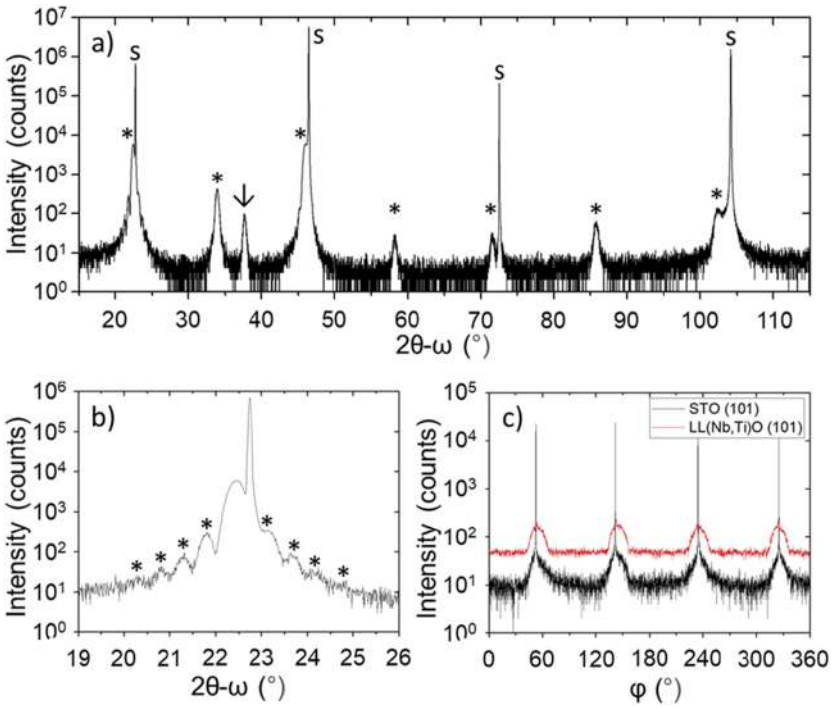

FIG. 2. (a) 2θ-ω pattern of LL(Nb, Ti)O-(Ti, Nb)O_2 grown on STO (001). Reflections are marked by * (00l) LL(Nb, Ti)O, → (Ti, Nb)O_2 (00l), and s STO (00l). (b) Kiessig thickness fringes of LL(Nb, Ti)O (002) reflection marked by *. (c) Overlapped φ scans of STO (101) (black) and LL(Nb, Ti)O (101) (red) reflections showing epitaxy.

our films performed with an out-of-plane geometry (top to bottom). Nyquist plots, of which a typical example at 25 °C is presented in Fig. 3(a), show a single semi-circle at a high frequency between 30 MHz and 10 kHz, and large capacitive response that begins to form a very resistive incomplete semi-circle at low frequencies. See the supplementary material, Fig. S1, for Nyquist plots displaying the low frequency response and temperature dependence of the EIS features. EIS data were modeled using the equivalent circuit in Fig. 3(a) (inset); R_{ion}/CPE_{ion} model the ionic conductivity of LL(Nb, Ti)O (with a capacitance of ~10^{-11} F cm^{-1}), which is in series with CPE_{dl},

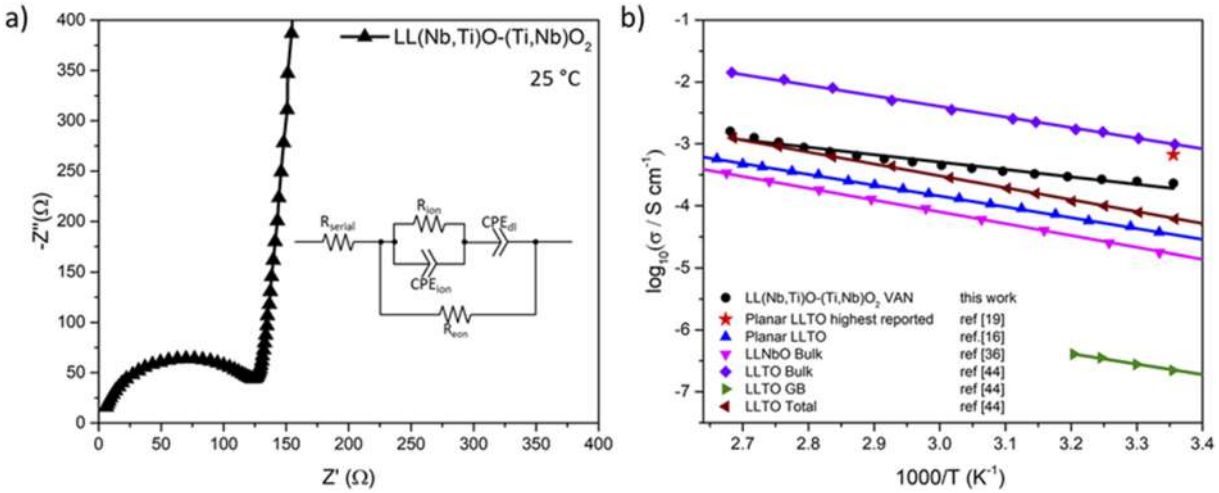

FIG. 3. (a) Typical Nyquist plot collected at 25 °C. Inset: the EIS model used to fit the data, where R_i/CPE_i corresponds to the ionic conductivity of LL(Nb, Ti)O, CPE_{dl} is the double layer, R_{eon} is the electronic pathway through the (Ti, Nb)O_2 columns, and R_{serial} contains contributions from the EIS setup, Nb-STO substrate etc. (b) Arrhenius plot of the LL(Nb, Ti)O-(Ti, Nb)O_2 VAN film in air displaying high ionic conductivity as compared to the literature results for planar LLTO PLD films,[16,19] powder LLTO,[44] and powder LLNO.[36]

the double layer capacitance; parallel to this is R_{eon}, the resistance contributed by the electronic pathway through the (Ti, Nb)O_2 phase; R_{serial} is the ohmic offset containing contributions from the Nb-STO substrate and internal resistances of the EIS setup (instrument, cabling, etc.).

LL(Nb, Ti)O-(Ti, Nb)O_2 VAN exhibits an ionic conductivity of 2.3×10^{-4} S cm^{-1} at 25 °C. The conductivity is thermally activated and obeys Arrhenius behavior [Fig. 3(b)] with an activation energy of 0.27 ± 0.01 eV, closely matched to the typically reported values of 0.30–0.40 eV for bulk LLTO/LLNO.[16,18,19,23,35,36] We note that several oxide ion-conductor VAN films exhibit lowered activation energies,[6,7,37] indicating that ions can move with less resistance through the nanocomposite system, as seen in our system.

The ionic conductivity observed here is higher than many LLTO PLD films[16,18,38,39] and comparable with the best reported planar LLTO films, which achieve 10^{-4} S cm^{-1} at room temperature.[19,40] Conduction is an order of magnitude higher than the bulk and grain boundary polycrystalline LLNO[23,35,36] and commensurate with single crystal studies on LLNO reports 10^{-4} S cm^{-1} at room temperature.[41] More in-depth single crystal studies show that ionic conductivity is anisotropic due to the tetragonal/orthorhombic crystal structure (dependent on Li content), with the (00*l*) orientation achieving 10^{-5} S cm^{-1}, increasing to 10^{-4} S cm^{-1} in the (*h*00) direction.[42] It is noted that the (00*l*) direction is probed in this study confirmed by 2θ-ω XRD scans presented in Fig. 2(a). Hence, an increase in an order of magnitude in conductivity along the (00*l*) axis in LL(Nb, Ti)O in the VAN films is observed, cf. bulk LLNO. However, we note that doping of titanium by niobium has been reported to increase the ionic conductivity of LLNO, because it allows for the phase to accommodate more lithium, thus resulting in more charge carriers available for conduction and an increased conductivity.[43] Thus, enhancement in ionic conductivity may not be exclusively caused by the VAN structure. However, an advantage that our VAN films have is the absence of grain boundaries; LLTO is known to suffer from low total conductivities as the grain boundary contribution is typically two orders of magnitude lower (10^{-5}–10^{-6} S cm^{-1}) than bulk ionic conduction.[20,22,44] Hence, the ionic conductivities of our LL(Nb, Ti)O-(Ti, Nb)O_2 VAN are higher than total conductivities of bulk LLTO [Fig. 3(b)]. Noting the high niobium content of our films, the

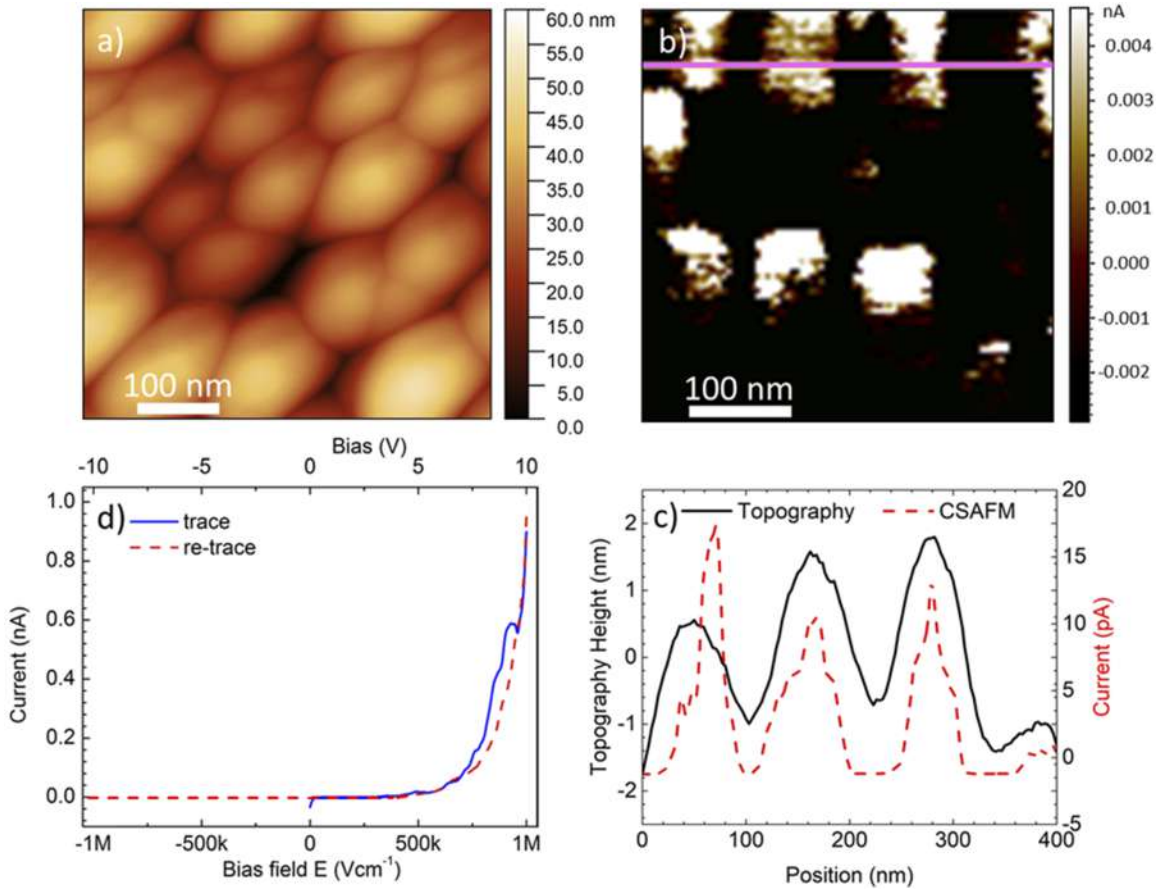

FIG. 4. (a) Tapping mode AFM topography images of LL(Nb, Ti)O-(Ti, Nb)O_2 nanocomposite films grown on Nb-STO (001). (b) CS-AFM image collected in the contact mode with the corresponding line scan (c) marked by the pink line. The accompanying topography image can be found in the supplementary material, Fig. S2. Columnar features clearly correspond with regions of high current. (d) IV curve collected with a 8 nm diameter CS-AFM tip positioned on a (Ti, Nb)O_2 column.

VAN is more robust when trying to achieve high ionic conductivities without painstaking optimization of PLD parameters for marginal enhancements in conductivity,[19] despite being a phase with lower conductivity in the powder form.[43,45]

To distinguish between regions of different charge carriers, we performed CS-AFM. The same columnar outgrowths seen in TEM are observed in the tapping mode AFM images [Fig. 4(a)], in agreement with the presence of Kiessig fringes in XRD [Fig. 2(b)], our films are very smooth, with the RMS roughness and peak to peak distances of 8.5 and 50.1 nm, respectively. Low roughness is essential for solid state batteries as it enables an intimate contact between the film and electrode materials, thus reducing the interfacial impedance to ionic diffusion across the electrode–electrolyte interface.[17] CS-AFM images [Fig. 4(b)] show distinct electronic conducting and insulating regions. Comparing these with the AFM line scans [Fig. 4(c)] and the height image (supplementary material Fig. S2), the topography and current profile clearly correlates with the protruding (Ti, Nb)O_2 features (as confirmed by TEM). Thus, these images are consistent with nanocolumns of an electronic conductor, the (Ti, Nb)O_2 anatase, embedded in the electrically insulating LL(Nb, Ti)O matrix.

To measure the electronic conductivity of a single (Ti, Nb)O_2 anatase column with CS-AFM, an IV curve was collected using an 8 nm diameter AFM tip positioned directly on a high conducting region [Fig. 4(d)]. By using a tip smaller in diameter than the (Ti, Nb)O_2 columns, we eliminate contributions from the LL(Nb, Ti)O matrix. The IV curve [Fig. 4(d)] is non-ohmic and exhibits high resistivities (3×10^5 Ω cm at 1 V). An IV curve collected using 300 μm electrodes as used in the EIS setup also exhibits similarly high resistivities (supplementary material, Fig. S3). The resistivities measured here are significantly higher than reported for Nb doped TiO_2 anatase (typically of the order 1–100 Ω cm as grown, enhanced to $<10^{-4}$ Ω cm with H_2 annealing[29,46]) and consistent with the presence of a rectifying contact in the VAN device. However, we note that, in practice, our VAN films have topography, which influences the AFM tip–sample contact, and there are several interfaces between the AFM tip, VAN film, and substrate all of which contribute to the as measured total resistivity of the device. For example, in TEM images (Fig. 1), there appears to be a thin LL(Nb, Ti)O layer underneath the (Ti, Nb)O_2 columns clearly seen in the Ti-EDX mapping image [Fig. 1(d)] and the overall EDX map (supplementary material, Fig. S4). LL(Nb, Ti)O forms a thin initial wetting layer on Nb-STO as their interfacial surface energy is very low due to being crystallography well matched (both are perovskites).[15] It is not clear how this layer contributes to the overall resistivity; hence, the measured (Ti, Nb)O_2 column resistivities should be taken as an upper limit and the true value is potentially several orders of magnitude smaller.

Despite the measured low electronic conductivities of our device, these measurements highlight several important considerations in order to build a successful VAN film battery with an interdigitated electrode/electrolyte; (1) work functions of the substrate/electrode should be well matched to prevent very resistive rectifying contacts; for example, it is widely reported that $SrRuO_3$ is required as a buffer layer between Nb-STO and $LiMn_2O_4$ to enable good electronic transport throughout the cathode device;[47,48] and buffer layers may be required for other electrode materials. (2) The quality of the VAN, as well as the pairing of the materials, is integral, because if the electrode component is not in contact with the current-collecting substrate, the device may not function. (3) It is difficult to eliminate intermixing in VAN, but it can be very detrimental to performance; hence, material combinations should be carefully chosen with intermixing in mind.

CONCLUSIONS

In this work, we have reported the first lithium-based VAN system composed of electrolyte–anode solid state battery materials deposited on widely available Nb-STO substrates. First, we have demonstrated that LL(Nb, Ti)O-(Ti, Nb)O_2 films can be grown epitaxially with high purity and crystallinity. The two phases are highly compatible with high interfacial crystallinity and no interface reactions. Thereafter, we demonstrated that the LL(Nb, Ti)O matrix exhibits a high Li^+ ionic conductivity of 2.3×10^{-4} S cm^{-1} at 25 °C with an activation energy of 0.27 ± 0.01 eV. The conductivity is an order of magnitude higher than bulk LLNO and comparable with the best available planar LLTO films. CS-AFM results show our VANs also contain distinct regions of electrically insulating [LL(Nb, Ti)O] and electronically conducting [(Ti, Nb)O_2] phases, a prerequisite for an interdigitated electrolyte/anode system. By showcasing all the essential physical properties, this work opens up the possibility of incorporating VAN films into an all solid-state thin film battery, either as electrodes or as electrolytes, by the pairing of suitable materials.

SUPPLEMENTARY MATERIAL

See the supplementary material for EIS of the low frequency arc, CS-AFM contact mode topography image, supplementary IV curves, and EDX map containing Ti, Sr, Nb, and La.

ACKNOWLEDGMENTS

J.L.M.-D. acknowledges the ERC advanced grant, EU-H2020-ERC-ADG No. 882929, EROS, and the Royal Academy of Engineering under Grant No. CIET1819_24. A.J.L. acknowledges support from EPSRC (EP/R513180/1). A.J.L. and J.L.M.-D. also acknowledge the EPSRC CAM-IES, Grant No. EP/P007767, for PLD time. S.D. and J.L.M.-D. acknowledge the EPSRC Faraday under Grant No. EP/T005394/1, FutureCat. This work was performed on the Royce Cluster Tool, part of the Cambridge Henry Royce Institute equipment, Grant No. EP/P024947/1, with equipment procured by Sir Henry Royce Institute—recurrent Grant No. EP/R00661X/1. Z.Q., Z.H., and H.W. acknowledge the funding support from the U.S. National Science Foundation for the TEM/STEM/EDX analysis at Purdue University (Grant Nos. DMR-1565822, DMR-2016453, and DMR-1809520).

AUTHOR DECLARATIONS

Conflict of Interest

The authors have no conflicts to disclose.

Author Contributions

The manuscript was written through contributions of all authors. All authors have given approval to the final version of this

manuscript. A.J.L. and J.L.M.-D. conceived the idea. A.J.L. wrote the draft of the manuscript before others contributed. Samples were grown by A.J.L.; XRD and AFM measurements were conducted by A.J.L.; CS-AFM measurements were conducted by A.K. and A.J.L.; EIS measurements were done by A.J.L.; and TEM and EDX were performed by H.W., Z.Q., and Z.H.

DATA AVAILABILITY

The data that support the findings of this study are available from the corresponding author upon reasonable request.

REFERENCES

[1] J. Janek and W. G. Zeier, Nat. Energy **1**, 16141 (2016).
[2] Q. Xia, S. Sun, J. Xu, F. Zan, J. Yue, Q. Zhang, L. Gu, and H. Xia, Small **14**, 1804149 (2018).
[3] J. F. M. Oudenhoven, L. Baggetto, and P. H. L. Notten, Adv. Energy Mater. **1**, 10–33 (2011).
[4] S. Ferrari, M. Loveridge, S. D. Beattie, M. Jahn, R. J. Dashwood, and R. Bhagat, J. Power Sources **286**, 25–46 (2015).
[5] J. W. Long, B. Dunn, D. R. Rolison, and H. S. White, Chem. Rev. **104**, 4463–4492 (2004).
[6] S. Lee, W. Zhang, F. Khatkhatay, H. Wang, Q. Jia, and J. L. MacManus-Driscoll, Nano Lett. **15**, 7362–7369 (2015).
[7] S. M. Yang, S. Lee, J. Jian, W. Zhang, P. Lu, Q. Jia, H. Wang, T. Won Noh, S. V. Kalinin, and J. L. MacManus-Driscoll, Nat. Commun. **6**, 8588 (2015).
[8] S. Lee and J. L. MacManus-Driscoll, APL Mater. **5**, 042304 (2017).
[9] J. Yoon, S. Cho, J.-H. Kim, J. Lee, Z. Bi, A. Serquis, X. Zhang, A. Manthiram, and H. Wang, Adv. Funct. Mater. **19**, 3868–3873 (2009).
[10] F. Baiutti, F. Chiabrera, M. Acosta, D. Diercks, D. Parfitt, J. Santiso, X. Wang, A. Cavallaro, A. Morata, H. Wang *et al.*, Nat. Commun. **12**, 2660 (2021).
[11] B. Zhu, G. Schusteritsch, P. Lu, J. L. MacManus-Driscoll, and C. J. Pickard, APL Mater. **7**, 061105 (2019).
[12] A. J. Lovett, M. P. Wells, Z. He, J. Lu, H. Wang, and J. L. MacManus-Driscoll, J. Mater. Chem. A **10**, 3478–3484 (2022).
[13] D. M. Cunha, C. M. Vos, T. A. Hendriks, D. P. Singh, and M. Huijben, ACS Appl. Mater. Interfaces **11**, 44444–44450 (2019).
[14] Z. Qi, J. Tang, S. Misra, C. Fan, P. Lu, J. Jian, Z. He, V. G. Pol, X. Zhang, and H. Wang, Nano Energy **69**, 104381 (2020).
[15] J. L. MacManus-Driscoll, Adv. Funct. Mater. **20**, 2035–2045 (2010).
[16] T. Ohnishi and K. Takada, Solid State Ionics **228**, 80–82 (2012).
[17] S. Kim, M. Hirayama, K. Suzuki, and R. Kanno, Solid State Ionics **262**, 578–581 (2014).
[18] F. Aguesse, V. Roddatis, J. Roqueta, P. García, D. Pergolesi, J. Santiso, and J. A. Kilner, Solid State Ionics **272**, 1–8 (2015).
[19] T. Ohnishi, K. Mitsuishi, K. Nishio, and K. Takada, Chem. Mater. **27**, 1233–1241 (2015).
[20] Y. Inaguma, C. Liquan, M. Itoh, T. Nakamura, T. Uchida, H. Ikuta, and M. Wakihara, Solid State Commun. **86**, 689–693 (1993).
[21] O. Bohnke, C. Bohnke, and J. L. Fourquet, Solid State Ionics **91**, 21–31 (1996).
[22] Y. Inaguma and M. Nakashima, J. Power Sources **228**, 250–255 (2013).
[23] K. Kawahara, R. Ishikawa, K. Nakayama, T. Higashi, T. Kimura, Y. H. Ikuhara, N. Shibata, and Y. Ikuhara, J. Power Sources **441**, 227187 (2019).
[24] S. Stramare, V. Thangadurai, and W. Weppner, Chem. Mater. **15**, 3974–3990 (2003).
[25] A. Belous, E. Pashkova, O. Gavrilenko, O. V'yunov, and L. Kovalenko, J. Eur. Ceram. Soc. **24**, 1301–1304 (2004).
[26] R. van de Krol, A. Goossens, and E. A. Meulenkamp, J. Electrochem. Soc. **146**, 3150 (1999).
[27] X. Yang, C. Wang, Y. Yang, Y. Zhang, X. Jia, J. Chen, and X. Ji, J. Mater. Chem. A **3**, 8800–8807 (2015).
[28] Y. Liu and Y. Yang, J. Nanomater. **2016**, 8123652.
[29] Y. Furubayashi, T. Hitosugi, Y. Yamamoto, K. Inaba, G. Kinoda, Y. Hirose, T. Shimada, and T. Hasegawa, Appl. Phys. Lett. **86**, 252101 (2005).
[30] T. Hitosugi, A. Ueda, S. Nakao, N. Yamada, Y. Furubayashi, Y. Hirose, T. Shimada, and T. Hasegawa, Appl. Phys. Lett. **90**, 212106 (2007).
[31] M. Lübke, J. Shin, P. Marchand, D. Brett, P. Shearing, Z. Liu, and J. A. Darr, J. Mater. Chem. A **3**, 22908–22914 (2015).
[32] C. Cavallo, G. Calcagno, R. P. de Carvalho, M. Sadd, B. Gonano, C. Moyses Araujo, A. E. C. Palmqvist, and A. Matic, ACS Appl. Energy Mater. **4**, 215 (2021).
[33] M. Wagemaker, W. J. H. Borghols, and F. M. Mulder, J. Am. Chem. Soc. **129**, 4323–4327 (2007).
[34] M. Madian, A. Eychmüller, and L. Giebeler, Batteries **4**, 7 (2018).
[35] S. García-Martín, J. M. Rojo, H. Tsukamoto, E. Morán, and M. A. Alario-Franco, Solid State Ionics **116**, 11–18 (1999).
[36] Y. Kawakami, M. Fukuda, H. Ikuta, and M. Wakihara, Solid State Ionics **110**, 187–192 (1998).
[37] Q. Su, D. Yoon, A. Chen, F. Khatkhatay, A. Manthiram, and H. Wang, J. Power Sources **242**, 455–463 (2013).
[38] K. K. Bharathi, H. Tan, S. Takeuchi, L. Meshi, H. Shen, J. Shin, I. Takeuchi, and L. A. Bendersky, RSC Adv. **6**, 61974–61983 (2016).
[39] D. H. Kim, S. Imashuku, L. Wang, Y. Shao-horn, and C. A. Ross, J. Cryst. Growth **372**, 9–14 (2013).
[40] J. Wei, D. Ogawa, T. Fukumura, Y. Hirose, and T. Hasegawa, Cryst. Growth Des. **15**, 2187–2191 (2015).
[41] Y. Fujiwara, K. Hoshikawa, and K. Kohama, J. Cryst. Growth **433**, 48–53 (2016).
[42] M. S. Ali, Y. Maruyama, M. Nagao, S. Watauchi, and I. Tanaka, Solid State Ionics **350**, 115330 (2020).
[43] L. Latie, G. Villeneuve, D. Conte, and G. Le Flem, J. Solid State Chem. **51**, 293–299 (1984).
[44] J.-F. Wu and X. Guo, Phys. Chem. Chem. Phys. **19**, 5880–5887 (2017).
[45] R. Gu, J. Kang, X. Guo, J. Li, K. Yu, R. Ma, Z. Xu, L. Jin, and X. Wei, J. Alloys Compd. **896**, 163084 (2022).
[46] H. Tang, K. Prasad, R. Sanjinès, P. E. Schmid, and F. Lévy, J. Appl. Phys. **75**, 2042–2047 (1994).
[47] K. Suzuki, K. Kim, S. Taminato, M. Hirayama, and R. Kanno, J. Power Sources **226**, 340–345 (2013).
[48] R. Hendriks, D. M. Cunha, D. P. Singh, and M. Huijben, ACS Appl. Energy Mater. **1**, 7046–7051 (2018).